New Journal of Physics
The open access journal at the forefront of physics

Deutsche Physikalische Gesellschaft DPG
IOP Institute of Physics

Published in partnership with: Deutsche Physikalische Gesellschaft and the Institute of Physics

OPEN ACCESS

RECEIVED
3 June 2016

REVISED
30 September 2016

ACCEPTED FOR PUBLICATION
25 October 2016

PUBLISHED
17 November 2016

PAPER

Acceleration of high charge-state target ions in high-intensity laser interactions with sub-micron targets

C McGuffey[1], A Raymond[2], T Batson[2], R Hua[1], G M Petrov[3], J Kim[1], C M Krauland[1], A Maksimchuk[2], A G R Thomas[2,4], V Yanovsky[2], K Krushelnick[2] and F N Beg[1]

[1] Center for Energy Research, University of California, San Diego, La Jolla, CA 92093-0417, USA
[2] Center for Ultrafast Optical Sciences, University of Michigan, Ann Arbor, MI 48109, USA
[3] Naval Research Laboratory, Plasma Physics Division, 4555 Overlook Ave. SW, Washington, DC 20375, USA
[4] Present address: Physics Department, Lancaster University, UK.

E-mail: cmcguffey@ucsd.edu

Keywords: ion acceleration, intense laser, ultrathin laser targets

Abstract

We have studied laser acceleration of ions from Si_3N_4 and Al foils ranging in thickness from 1800 to 8 nm with particular interest in acceleration of ions from the bulk of the target. The study includes results of experiments conducted with the HERCULES laser with pulse duration 40 fs and intensity 3×10^{20} W cm^{-2} and corresponding two-dimensional particle-in-cell simulations. When the target thickness was reduced the distribution of ion species heavier than protons transitioned from being dominated by carbon contaminant ions of low ionization states to being dominated by high ionization states of bulk ions (such as Si^{12+}) and carbon. Targets in the range 50–150 nm yielded dramatically greater particle number and higher ion maximum energy for these high ionization states compared to thicker targets typifying the Target Normal Sheath Acceleration (TNSA) regime. The high charge states persisted for the thinnest targets, but the accelerated particle numbers decreased for targets 35 nm and thinner. This transition to an enhanced ion TNSA regime, which more efficiently generates ion beams from the bulk target material, is also seen in the simulations.

1. Introduction

Among the prime interests in studying relativistic laser–plasma interactions are compact beam sources of high-quality energetic ions having desirable parameters, namely energy extending to 10 s of MeV nucleon^{-1}, micrometer-scale source size, directionality, and sub-picosecond source duration. The mechanism for ion acceleration accessible with the previous generation of lasers has been restricted to Target Normal Sheath Acceleration (TNSA) [1, 2]. TNSA takes place when a foil is irradiated by a laser intense enough to produce 'hot' electrons with enough energy to transit the target. These hot electrons concentrate opposite the irradiated side of the target, forming a sheath and associated field that can reach strength of order TV/m causing atoms located in the substrate and in surface contaminant layers of hydrocarbons and H_2O to become ionized and subsequently accelerated. However, the TNSA mechanism has the issue of a slow scaling for maximum ion energy, E_{max}, versus laser intensity, I, of $I^{1/3}$ to $I^{1/2}$ for relativistically intense lasers [3, 4] although it has been observed [5] to scale as much as linearly with power for ultrashort pulses at intensity $>10^{21}$ W cm^{-2}. Furthermore, the sheath field in TNSA is confined to a Debye length in the dimension perpendicular to the target surface and can thus only accelerate those ions initially residing a few nanometers from the initial target/vacuum interface, i.e. H^+, $C^{(1-6)+}$, and $O^{(1-8)+}$, and the produced ion beams are typically characterized by large divergence and broad continuous energy spread.

As the target is made thinner, the hot electrons reaching the target rear are greater in population and energy and they recirculate [6], enhancing the sheath strength and increasing ion acceleration. For example, the maximum energy and conversion efficiency of proton beams have been observed in experiments [7, 8] to scale inversely with thickness for targets with multi-μm scale. However, the mechanism becomes ineffective if the

target becomes thin enough that a shock, triggered from any unwanted pre-pulses present in the rising edge of the main laser pulse, breaks out from the rear surface before peak laser intensity [9, 10]. Further, for a target nearly as thin as the relativistic skin depth, $l_s = \gamma c/\omega_{pe}$, the laser field itself can reach the target rear surface directly which could change the effectiveness of TNSA and/or enable other mechanisms. For targets thinner than the non-relativistic skin depth, c/ω_{pe}, ions undergo Coulomb explosion [11], which also results in large divergence and broad continuous energy spread but greater maximum energy.

For the intermediate transitional region, where the target thickness is comparable to the relativistic skin depth, several mechanisms have been proposed and observed experimentally including radiation pressure acceleration [12, 13], breakout afterburner [14], relativistic transparency [15], directed Coulomb explosion [16], magnetic vortex acceleration [17], and collisionless shock acceleration [18]. These regimes may be accessed using a combination of ultraintense, ultrahigh contrast laser, and sub-micron thick targets and are expected to give superior performance in terms of energy scaling, laser-ion conversion efficiency and narrow-band energy spectrum. Additionally, these mechanisms hold promise for accelerating the bulk of the target thereby extending the options for ion beam constituents to any solid that can be made thin enough. While the boundaries and capabilities of these mechanisms have been explored for protons and carbon ions [19–22], few experimental works with laser intensity $>10^{20}$ W cm^{-2} have focused on the acceleration of heavier ions (having atomic number, Z, $\gg 6$), because the ion species are less prevalent than the protons. The notable exceptions are an early investigation with the 400 J VULCAN petawatt laser [23] in which ^{56}Fe ions were accelerated to 10 MeV nucleon^{-1}, a recent paper showing acceleration of Al^{11+} ions from aluminum targets with a peaked spectrum, narrow charge state distribution and fluence comparable to that of the protons [24] using an 80 J laser, and acceleration of Au to intermediate charge states using a similar but lower intensity laser compared to this work [25].

In TNSA of contaminant ions, the species that are accelerated to high energy are typically those ionized to a fully or nearly fully stripped state, producing few charge states in the beam, e.g. H^+, $C^{(5-6)+}$, and $O^{(7-8)+}$. However, acceleration of high Z target ions has an additional layer of complexity due to field and collisional ionization which lead to space- and time-dependent charge state distributions. Efficient acceleration relies on producing highly charged species overlapped in space with the strongest accelerating field; it has been shown that matching the target material with a given laser intensity is key to high energy acceleration for this reason [26]. This additional layer of complexity means the best parameters for accelerating protons are not necessarily best for accelerating high Z ions. Therefore we have conducted experiments and particle-in-cell simulations of ultraintense laser–solid interactions in the transitional regime with particular attention paid to the acceleration of ions from the target bulk material.

In this work, we show that laser contrast and target thickness, which are well-known key parameters in laser acceleration of protons, are even more critical in the acceleration of ions from the bulk of the target. The production of multi-MeV ions from the target bulk material was markedly increased for thickness <200 nm. We established an optimum target thickness range of 50–150 nm for the acceleration of contaminant and bulk ions including a Si beam of predominantly Si^{12+} charge state.

2. Experimental setup

The experiments were carried out using the HERCULES Ti: sapphire laser system [27] with pulse duration 40 fs full-width at half maximum (FWHM), peak intensity 3×10^{20} W cm^{-2}, and energy contrast of 10^{-6} between the main pulse and the amplified spontaneous emission (ASE) on the nanosecond timescale. Two parallel plasma mirrors enhanced the energy contrast before the arrival time of the main pulse by an additional factor of $\sim 3 \times 10^{-4}$ as reported previously [28]. The laser focal spot was optimized using a wavefront flattening routine and deformable mirror immediately preceding the $f/3$ off-axis paraboloid. Compared to previous experiments with the same laser and similar setup [28, 29], the focal spot size, 4.1 μm FWHM, was 3.4$\times$ larger and the intensity was lower by an order of magnitude. It was hypothesized that the reduced transverse gradients would prevent target breakup and acceleration disruption. The linearly polarized laser was incident normal to flat targets of Si_3N_4 with thickness 8, 15, 35, 50, 150, 200, or 500 nm, or Al with thickness 200, 500, 800, or 1800 nm.

The laser contrast on each shot was monitored in two ways. First, a fast photodiode (250 ps rise-time) and 2 GHz oscilloscope recorded the pulse shape transmitted through the first turning mirror shown in figure 1, preceding the plasma mirrors. Example traces are shown in figure 2(a). Second, the mid-field of the laser was monitored downstream of the plasma mirrors by partially focusing the portion transmitted through a turning mirror. Shots with no measurable prepulse and smooth mid-field (see figure 2(c)) were presumed to be free of prepulses capable of target damage on the nanosecond timescale. For some shots the mid-field was uneven with spatial modulations (see figure 2(b)). When a measurable prepulse on the photodiode was also observed, this was presumed to be due to early breakdown of the plasma mirrors, and other times it may have been due to

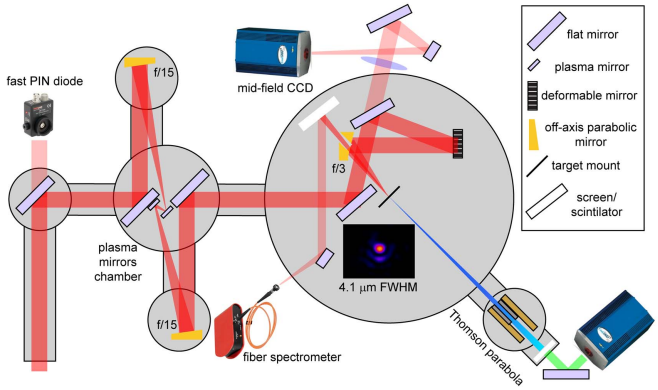

Figure 1. Experimental chamber configuration. After leaving the compressor, the HERCULES laser pulse is focused into the dual plasma mirror chamber, recollimated and sent into the experimental chamber. The last two optics are a full-aperture deformable mirror and $f/3$ off-axis paraboloid.

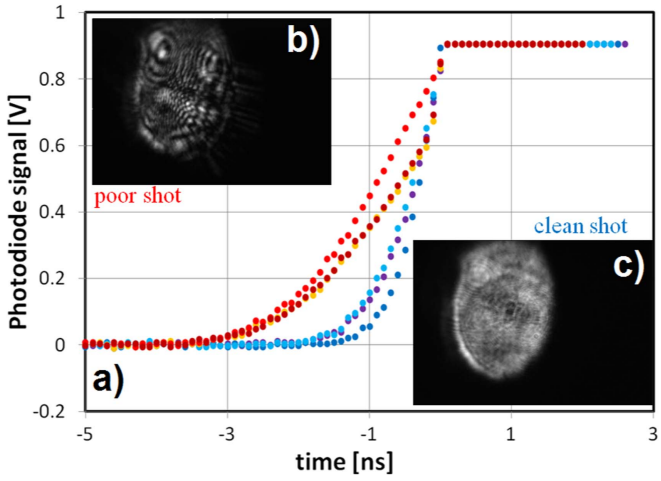

Figure 2. Contrast diagnostics show two distinct regimes of prepulse. For shots with noticeable prepulse energy on the nanosecond timescale ((a), red tones), the plasma mirror was triggered early resulting in modulation of the beam profile downstream (b). When the prepulse energy was properly suppressed in the front end ((a), blue tones), the beam profile was smooth (c).

stochastic damage on the plasma mirror from neighboring shots. These shots were rare and more likely to occur after several hours of laser operation due to laser drift issues. The analyzed data presented in this work do not include these shots. A Thomson parabola (TP) ion spectrometer with detector arrangement consisting of a microchannel plate, scintillator, and optical CCD camera was aligned to the target rear normal to record the spectra of ion species with distinct charge:mass ratios (q/m).

3. Ion acceleration measurements from sub-micron targets

An example raw datum from the TP is shown in figure 3 for a Si_3N_4 target with thickness 150 nm. The bright quadrant at the top-right shows the straight-through or infinite energy point and energy spectra for different q/m ions fan out in parabolic traces to the lower left. The top spectrum is that of protons, H^+, followed by $^{12}C^{6+}$ or other fully stripped ions with equal q/m ratio. Ions which are not fully stripped fall below this trace. Signals from H^+ and $^{12}C^{(1-6)+}$ were prevalent in all shots as no effort was made to remove contaminants from the target *in situ*. Several more spectra are visible from ^{28}Si and ^{14}N, which overlap with the even Si traces. The circular aperture defining the lowest detectable energy is due to the size of the circular microchannel plate. The maximum energy observed on the TP is not necessarily a hard cut-off, just the maximum energy before the signal cannot be distinguished from noise. Detection of ions was strongly dependent upon laser contrast. Figures 4(a), (b) and (d), (e) compare the TP data for two different target types when prepulse was detected (poor contrast as defined above) or was below the detectable level. When contrast was poor, proton maximum energy, ion charge and number of charge states were all reduced substantially. These outcomes may be the result of

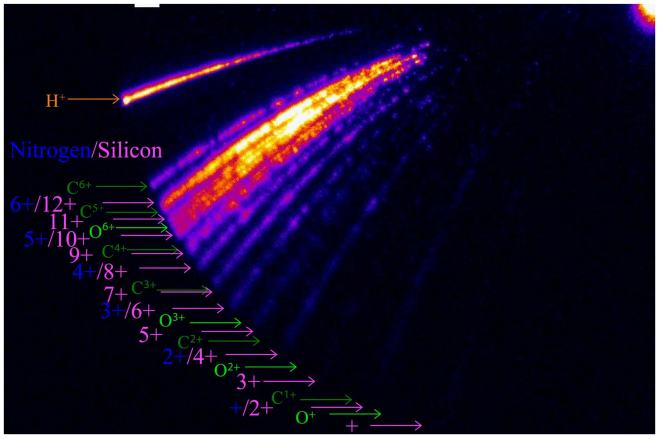

Figure 3. An example raw datum from the Thomson parabola with 15 clear charge-to-mass traces. In this particular datum from a 150 nm Si_3N_4 target four charge states of C and $Si^{(10-11)+}$ can be distinguished by eye.

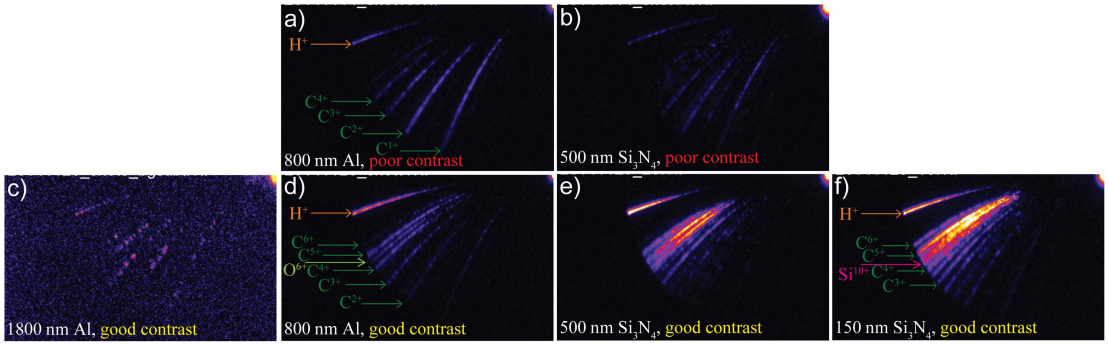

Figure 4. TP data from six shots with varying thickness and material exhibitting the general dependence upon contrast and target thickness. Subfigures (a) and (b) are from shots with 'poor contrast', as defined in the text and (d) and (e) are from shots with the same thicknesses and 'good contrast'. (c) is from a thicker Al target (the color scale has been reduced for compared to the other five images), and (f) is from a thinner Si_3N_4 target. As target thickness was decreased there was a transition from weak acceleration of only contaminants to higher signal and numerous species.

prepulse directly disrupting the target or triggerring the plasma mirrors early leading to degradation of the main pulse focus on target.

The ion beam charge and species distribution were strongly dependent upon target thickness. As shown in figure 4(c) relatively thick Al (1800 nm) samples resulted in only protons and very low charge of C contaminants. As the target was changed to thinner Al (d) and even thinner Si_3N_4 (e) and (f), the H^+ signal first increased down to 50 nm then stabilized and the signals from Si and N increased.

3.1. Contaminant species

Among Si_3N_4 targets with thickness between 8 and 500 nm the proton and C contaminant ion beam parameters were maximum for foil thickness 35–50 nm. Proton and carbon species traces from the TP data for individual trials at various thickness are plotted in figure 5. The maximum detected energy was greatest for target thickness of 35 nm with 4 MeV for protons. C ion energy peaked for 50 nm thickness: 1.2 MeV nucleon^{-1} for C^{6+} and 0.7 MeV nucleon^{-1} for C^{4+}. The total contaminant ion energy and particle numbers were greater than those from thicker Al foils; energy was greatest for 50 nm targets and particle number decreased sharply as thickness was reduced below 50 nm.

3.2. High charge-state ions from the target bulk

For ions from the bulk, Si^{q+} and N^{q+}, where q is any charge state, an optimal target thickness was also observed. The signals from intermediate charge states, such as Si^{7+}, were about the same for thickness 500 − 50 nm and diminished for 35 and 8 nm as shown in figure 6(a). Si^{6+}, which does not overlap with any carbon or oxygen states, displayed the same trend. The higher charge states, however, were significantly less abundant and energetic for the thickest targets as shown in figure 6(b). The higher charge states have a higher minimum

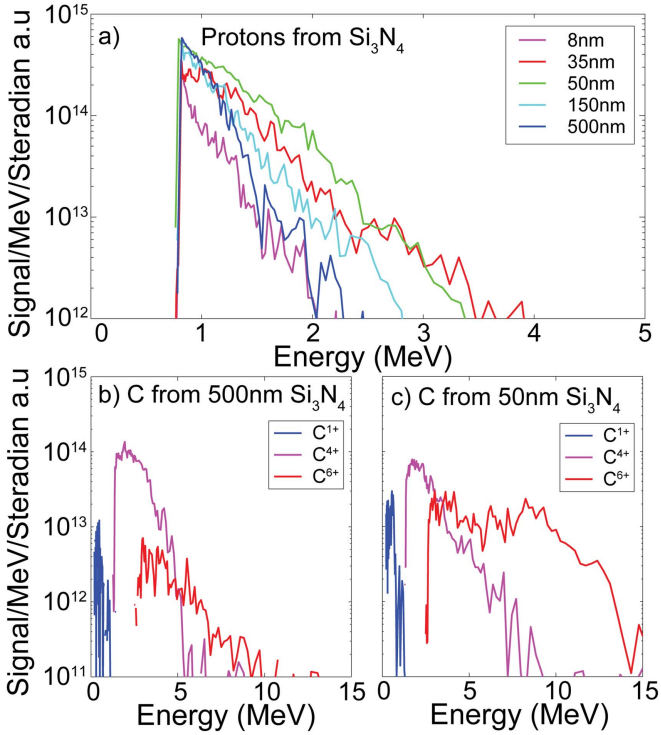

Figure 5. Contaminant ion spectra from Si_3N_4 targets of all thicknesses. (top) The proton spectrum peaked for 35–50 nm. (bottom) For thick targets all charge states of carbon were present, but C^{6+} signal increased as thickness was reduced.

detected energy (due to the circular detector shape) and higher maximum energy due to their higher q/m ratio. The maximum energies were 0.3 MeV nucleon^{-1} for Si^{7+} and 0.8 MeV nucleon^{-1} for Si^{11+}, which are slightly lower than the values reported above for C^{4+} and C^{6+} having slightly higher q/m ratios. Note that Si^{11+} charge states has been selected for presentation in figure 6 because it has distinct q/m ratio from any nitrogen, carbon, or oxygen states. The experimental data show that bulk ions such as Si^{+q} and N^{+q} can be accelerated if the target is sufficiently thin.

Species distributions as derived from the TP data analysis are shown in figure 7. Trace positions for each species of interest were determined by manually adjusting parabolas for each species and using the same position for all shots. The trace data, which have dimensions of (counts)/MeV/steradian, were integrated over energy between the lower cutoff and a chosen maximum energy. The fractional signal plotted in figure 7 is the fraction of a particular trace's integrated signal divided by the sum over all traces of the same element. In most cases the distributions were indistinguishable when the upper integral bound was chosen to be 5 MeV or infinite energy.

As target thickness was decreased the distribution of charge states shifted from low to high for both bulk (Si) and contaminants (C) ions. As shown in the left column of figure 7, for 500 nm thickness, the distributions for silicon and carbon were nearly symmetrically centered on charge states 10+ and 4+, respectively. For 35 nm thickness, only silicon states $Si^{(10-12)+}$ were present with >10% of the fractional signal and the Si^{12+} state (He-like) dominated. Si^{13+} was not observed.

The reason for this single dominant charge state is the large step in ionization potential between the Si^{12+} and Si^{13+} states, causing a bottleneck in the ionization progression. Table 1 lists the ionization potentials [30] and required laser field and intensity to reach each charge state of silicon through above-threshold field ionization [31]. The intensity of the laser, the strongest field present in the system and corresponding to an electric field of 46 MV μm^{-1}, is much greater than the field ionization threshold intensity for reaching Si^{12+} (2×10^{18} W cm^{-2}), but far below the threshold for Si^{13+} (8×10^{20} W cm^{-2}). Therefore on the front side of the target, generation of Si^{12+} is expected to be widespread. The TNSA field on the rear side of the target has maximum electric field strength $\epsilon = 4.8$ MV μm^{-1} based on the maximum proton energy according to estimates with a plasma expansion model [2, 32]; the maximum energies of $C^{4+,6+}$, and $Si^{7+,11+}$ indicate that they experienced maximum longitudinal fields in the range $1.0 < \epsilon < 2.2$ MV μm^{-1}. With these field strengths on the rear side, Si^{12+} can just barely be produced. However, the 35 nm targets are thinner than the relativistic skin depth so evanescent transmission of the laser can increase the number of high charge states born at the back of the target, in position to be accelerated by the sheath.

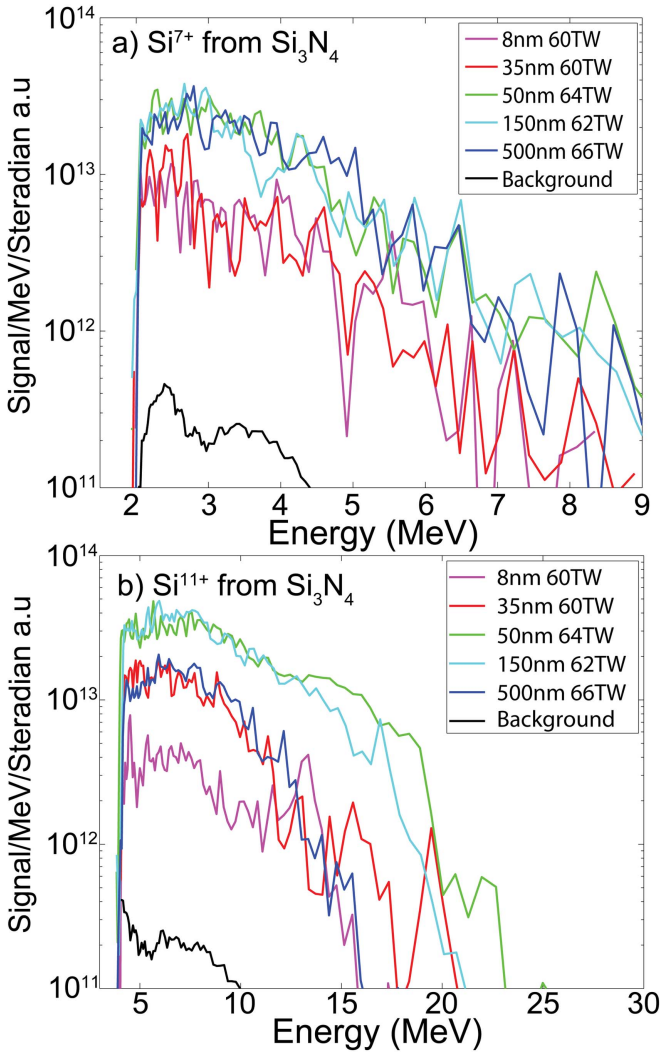

Figure 6. Spectra of ions from the bulk. (top) $^{28}Si^{7+}$ was detected even for the thick 500 nm target. (bottom) The high charge state $^{28}Si^{11+}$ was significantly less abundant and energetic for the thick target. The 11+ charge state ions reached three times higher maximum energy than the 7+ ions. The Si spectra peaked for thickness 50–150 nm. Background traces have been included from a datum in which the laser energy was anomalously low and no ion species were observed.

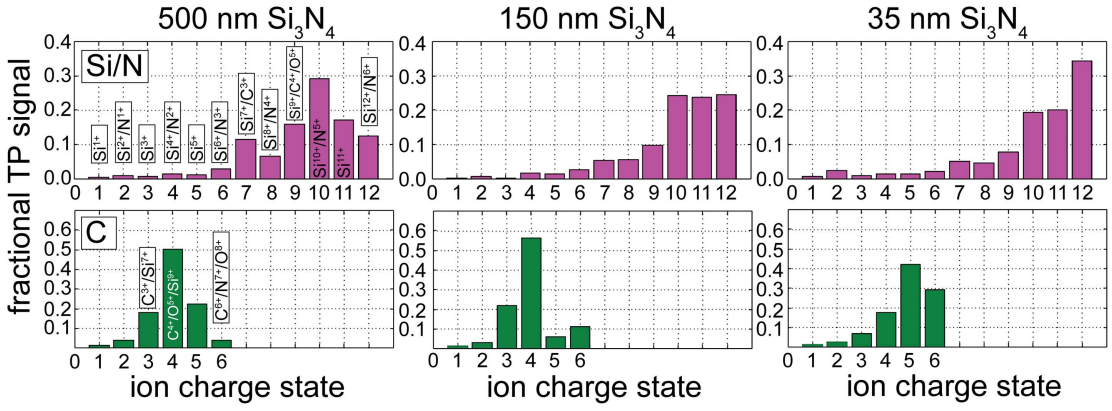

Figure 7. Charge state distributions from TP data for Si target ions (top) and C contaminant ions (bottom) from thick (left) and thin (right) Si_3N_4 targets. Multiple species are listed when they cannot be discriminated due to closely matching q/m.

Table 1. Ionization characteristics for the charge states of Si, including the ionization potential to reach state q and the field E_{Th} and corresponding intensity I_{Th} for barrier suppression ionization.

q	1	2	3	4	5	6	7	8	9	10	11	12	13	14
I_{p} (eV)	8.152	16.346	33.493	45.142	166.771	205.058	246.530	303.179	351.111	401.436	476.075	523.511	2437.740	2673.178
E_{Th} (V cm^{-1})	1.15×10^{8}	2.32×10^{8}	6.49×10^{8}	8.85×10^{8}	9.66×10^{9}	1.22×10^{10}	1.51×10^{10}	2.00×10^{10}	2.38×10^{10}	2.80×10^{10}	3.58×10^{10}	3.97×10^{10}	7.94×10^{11}	8.87×10^{11}
I_{Th} (W cm^{-2})	1.76×10^{13}	7.13×10^{13}	5.59×10^{14}	1.04×10^{15}	1.24×10^{17}	1.96×10^{17}	3.01×10^{17}	5.28×10^{17}	7.50×10^{17}	1.04×10^{18}	1.70×10^{18}	2.08×10^{18}	8.35×10^{20}	1.04×10^{21}

In combination with this bottleneck effect, ions ionized to the highest charge state receive the strongest acceleration from fields and are therefore more likely to reach the detector. For silicon this leads to dominance of the He-like state. Carbon can be fully stripped with threshold intensity 6×10^{18} W cm^{-2}, and states $C^{(5-6)+}$ are prevalent in the data.

4. Particle-in-cell simulations

Simulations of the short pulse interaction were conducted with a two-dimensional particle-in-cell (2D PIC) code written at the Naval Research Laboratory [33]. A laser with parameters chosen to match the HERCULES experiments (40 fs, 3.0×10^{20} W cm^{-2}, 4.1 μm FWHM spot, 0.8 μm wavelength) was injected into a 100×128 μm (length $\times$ width) box and incident normally onto a 3.2 g cm^{-3} slab of Si_3N_4. The target thickness was varied from 10–500 nm, and 5 nm thick layers of CH contaminant was added directly on both the front and rear sides of all targets. The cells were 20 nm squares with 38/50/42 particles per cell for species Si/N/C.

In order to correctly predict the ion charge distribution, an ionization dynamics model is added to the PIC code, which works as follows. At the beginning of the simulations all computational particles representing the various species of the target (Si, N, etc) are initialized with charge +1. A corresponding amount of electron computational particles is added to conserve quasineutrality. During the simulations the charge of each species except for hydrogen is dynamically incremented due to tunneling and collisional ionizations. Tunneling ionization is modeled using the Ammosov–Delone–Krainov ionization rate equation [31, 34]. It is applied for each ion using the electric field strength at the location of the (ion) computational particle. The collisional ionization rates are calculated using cell-averaged electron density, energy and velocity, and ionization cross section based on the Lotz formula [35]. The latter has the advantage of being universal and computationally effective, although the degree of accuracy may vary depending on the ion charge state and atomic number [36]. Once computed, the tunneling and collisional ionization rates are tested for 'ionization events' for every computational particle at every time step using a standard Monte Carlo scheme [36, 37]. If tested positive, i.e. a new ionization event occurs, the ion charge is incremented and a new electron computational particle is added at the location of the ion. Following this procedure, every computational particle acquires its own charge, which evolves in time. By counting the number of charges for each species, the charge distribution function is built.

Figures 8(a) and (b) show the time-histories of laser intensity and energy in the system for a 50 nm Si_3N_4 target. About 80% of the laser energy is reflected and eventually leaves the domain. This value is high because there is no assumed preplasma and this 50 nm thick target remains opaque throughout the interaction. The energy that gets absorbed is given to particles, most rapidly to electrons which peak at about 10% of the laser energy at time $t = 60$ fs. The electron energy then decreases as energy is given to ions. Protons gain energy most rapidly, while the other ions gain energy later and more slowly. Carbon and nitrogen gain energy concurrently, and Si ions gain energy least rapidly. This behavior is consistent with sheath acceleration in which the highest q/m ratio species lead the expansion and shield trailing species reducing the field they experience. Figures 8(d)–(f) plot the spectra of electrons 40 fs into the simulation (when the intensity on target is greatest) and four different ion species at the end of the simulations (240 fs). In total, protons are the most numerous single species in the forward directions (2.3×10^{11} ions sr^{-1}), but the target ions Si^{q+} (1.8×10^{11} ions sr^{-1}) and N^{q+} (3.3×10^{11} ions sr^{-1}) combined have higher charge and total energy than the contaminants p^+ and C^{q+} (1.4×10^{11} ions sr^{-1}).

The charge state distributions of Si and C ions traveling within 10° of the forward target normal direction for three target thicknesses are shown in figure 9. As in the experiment, the degree of ionization increases as target thickness is reduced for both bulk target (Si and N) and contaminant (O or C) ions. For the thick target simulation, the Si charge states are broadly distributed while the C ions have mostly reached He-like to fully stripped states. As the target thickness decreases to 150 nm, the Si distribution shifts slightly higher and then for 35 nm thickness it becomes dominated by the He-like state. The charge states $Si^{\leqslant 10+}$ and Si^{14+} disappear from the forward direction. The fractional populations of $C^{(4-5)+}$ ions decrease and the fraction reaching full ionization increase to nearly 90% for both the 150 and 35 nm thickness cases. This behavior is in agreement with the changes observed experimentally in figure 7 whereby the Si ionization is bottlenecked to the He-like state and the C reaches full ionization.

In the simulations of a 150 nm target, Si^{12+} ions from the front side do not reach the rear of the target. In the simulation of a 35 nm target the front of the target is observed to be pushed by hole-boring [38, 39]. Si ions ionized and accelerated by the laser are pushed forward and are able to reach the TNSA field at the rear. Because these ions felt the laser field directly, many of them (~90% of those within the focal spot) attain the maximum ion charge allowed by field ionization (Si^{12+}), and by reaching the TNSA sheath they are able to be accelerated directionally toward the detector.

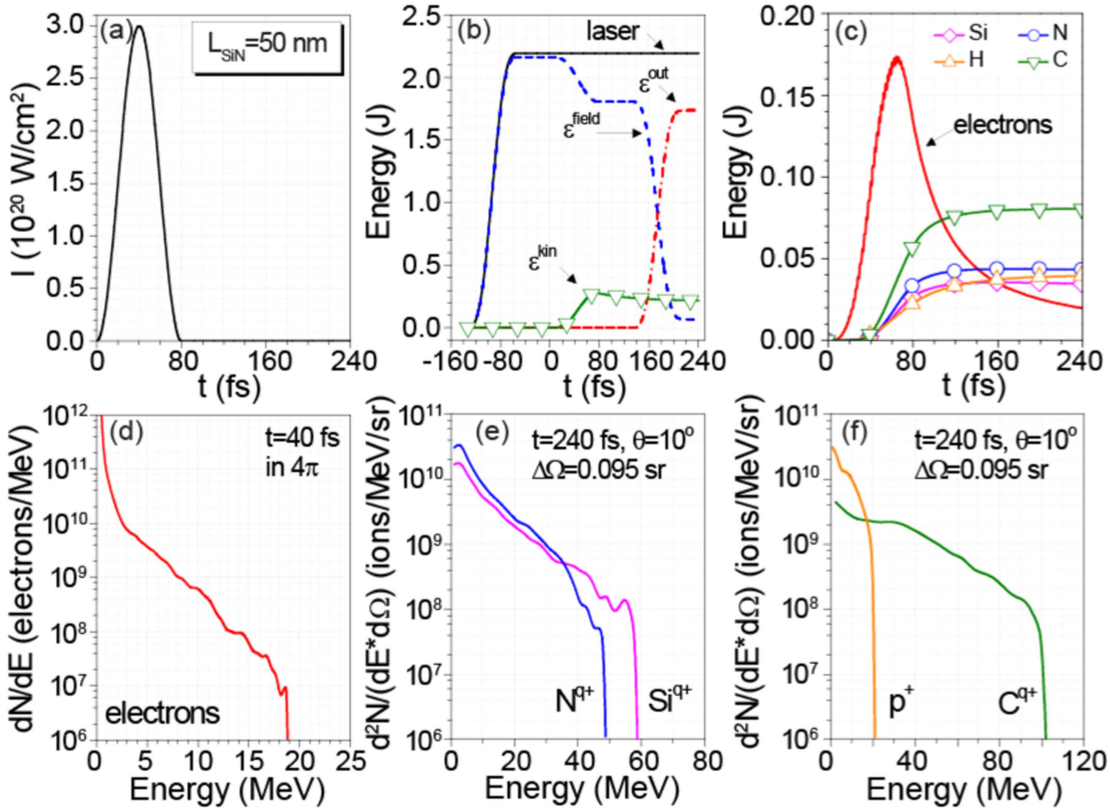

Figure 8. Numerical simulations of a 50 nm Si_3N_4 target. (a) the input laser intensity temporal profile; (b) the energy balance between total field energy and the sum of kinetic energy for all particles; (c) the kinetic energy for all particle among five different species; (d)–(f) the spectra of electrons, ions from the bulk, and contaminant ions through 240 fs of simulation time.

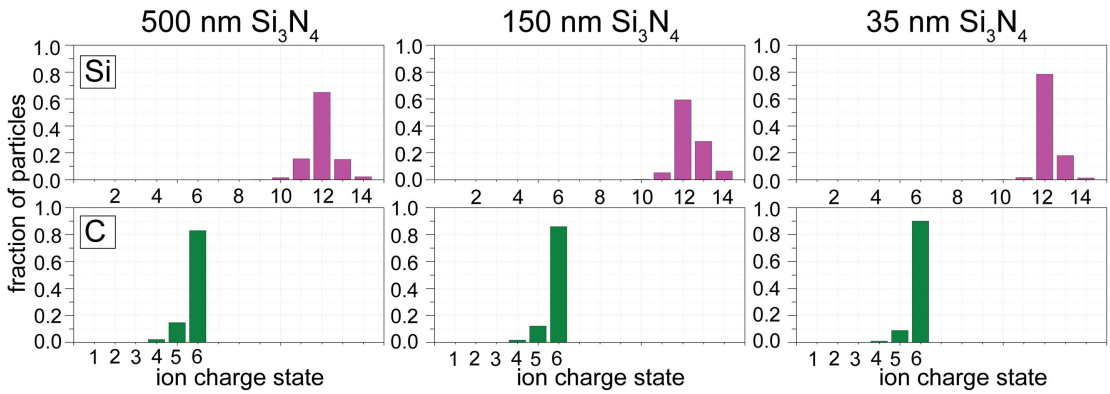

Figure 9. Charge state distributions from PIC simulations for Si (top) ions from the bulk and C contaminant ions (bottom) from 500, 150, and 35 nm thick (left to right) Si_3N_4 targets. Only ions within 10° of the target normal are included. Laser parameters are the same as in figure 8.

This observation fits in with a theoretical consideration of hole-boring. The normalized hole-boring velocity is $v_{hb}/c = \sqrt{\frac{I}{m_i n_i c^3}}$ and the hole-boring length is $l_{hb} = v_{hb}\tau_{FWHM}$, where c is the speed of light, m_i and n_i are the ion mass and density, and τ_{FWHM} is the laser pulse duration. For the parameters of the experiment, $v_{hb}/c \approx 0.004$, but since the laser pulse is so short, $l_{hb} \approx 50$ nm. This is consistent with the observation of hole-boring in the 35 nm simulation.

A secondary effect can also be seen in the simulation results—there is a small fraction of $Si^{(13-14)+}$ ions present for the 500 and 150 nm cases whereas none were observed experimentally. As discussed earlier, these states cannot be produced by field ionization. It is seen that in the simulation they arise from collisional ionization within the target, taking place after the laser has been reflected. When collisional ionization was

turned off in a test simulation the charge states $Si^{(13-14)+}$ disappeared from the forward direction. For thinner targets, there are fewer collisions in the target and therefore fewer chances for Si^{12+} ions to be further ionized. This leads to further narrowing in the charge state distribution for the thinnest target.

5. Conclusions

The ion behaviors are similar to previously discovered trends and expectations from theoretical treatments of the TNSA mechanism for protons. For example, the maximum energy and conversion efficiency of proton beams have been observed in many experiments [7, 8, 40] to scale inversely with thickness for targets with multi-μm scale and reverse trend sharply below some optimum thickness. For typical experiments this reversal is due to a shock wave from the nanosecond-scale ASE prepulse that can transit through a multi-μm target prior to the main pulse arrival and disrupt the rear target surface [9], reducing the sheath strength and ultimately reducing signal and maximum energy of any sheath-accelerated ions. For experiments believed to be free of ASE (e.g. [40] and this work), the optimal thickness can be expected to be sub-μm.

In our work targets had thickness of order of the relativistic skin depth and thinner, so the optimal thickness was determined by the tradeoff between maximum sheath strength and laser transmission [41]. For heavy ions, this optimum is convolved with the trend of increasing achievable ionization state with thinner targets. The electron density in Si_3N_4 is 1000$\times$ the classical critical density. The interaction volume, which is a flat disk for these thin targets,would have to expand in thickness to several microns in order to become transparent; such expansion cannot occur in the sub-picosecond timescale. However, the relativistic skin depth is 45 nm for the Si_3N_4 targets at the intensity in the experiment. For targets thinner than this the intense laser can deliver a strong electric field that interacts throughout the bulk of the target, sustaining the ionization process, but for the thinnest targets (8 nm) laser energy is wasted. This explains the observed trends (1) that increased charge state continued down to the thinnest target in both experiment and simulation and (2) the maximum energy and particle number decreased by as much as factors of 2 and 10, respectively for both target and contaminant species below 50 nm in the experiment (see figures 5(a) and 6).

Regarding the broader charge distribution observed in the experimental data, we surmise that the Gaussian distribution of laser intensity in the transverse direction prescribed in the simulations leads to a sharp focal spot having exclusively Si^{12+} and just a few ions with lower charges in the fringes of the focal spot. That is why in the simulations we observe mostly Si^{12+} and some $Si^{(10\&11)+}$. The experimental profile had a more complex shape in the transverse direction including two partial Airy rings with larger annular area than the circular main spot but much lower intensity (see figure 1 inset). Therefore, it is fitting that in the experiment more ions with lower charges were observed than in the simulation. The species $Si^{(13\&14)+}$ could only be produced by Si^{12+} ions from the front-side undergoing collisional ionization while traveling in the forward direction in the target. These species were detected in the simulations only when collisional ionization was modeled, and they had low quantity due the limited thickness for collisions to occur.

In summary, we have shown that laser contrast and target thickness are critical parameters in the acceleration of ions from the bulk of modest-Z targets. While these are well-known to be critical in proton acceleration, acceleration of target ions also depends on matching the target material to the field strength of the laser and rear sheath. The production of multi-MeV target ions was markedly increased for thickness $<$200 nm. The optimum target thickness was 50–150 nm for the acceleration of both contaminant and bulk target ions. In this range, the ion beam particle number and maximum energy were maximized. The optimal range occurs when the target is thin enough to recirculate hot electrons, producing a strong target normal sheath yet thick enough that laser energy is not wasted by evanescently transmitting. The degree of isolation of the C^{6+} and Si^{12+} states was however greatest for 35 nm thickness, less than l_{hb} and l_s, when the laser can push ions and ionize them all the way to the rear of the target.

Acknowledgments

This work was performed with the support of the Air Force Office of Scientific Research under grant FA9550-14-1-0282. GMP would like to acknowledge the DoD HPC computing program at NRL.

References

[1] Wilks S C, Langdon A B, Cowan T E, Roth M, Singh M, Hatchett S, Key M H, Pennington D, MacKinnon A and Snavely R A 2001 *Phys. Plasmas* **8** 542
[2] Mora P 2003 *Phys. Rev. Lett.* **90** 185002
[3] Beg F N, Bell A R, Dangor A E, Danson C N, Fews A P, Glinsky M E, Hammel B A, Lee P, Norreys P A and Tatarakis M 1997 *Phys. Plasmas* **4** 447

[4] Krushelnick K, Clark E L, Beg F N, Dangor A E, Najmudin Z, Norreys P A, Wei M and Zepf M 2005 *Plasma Phys. Control. Fusion* **47** B451
[5] Zeil K, Kraft S D, Bock S, Bussmann M, Cowan T E, Kluge T, Metzkes J, Richter T, Sauerbrey R and Schramm U 2010 *New J. Phys.* **12** 045015
[6] Mackinnon A J, Sentoku Y, Patel P K, Price D W, Hatchett S, Key M H, Andersen C, Snavely R and Freeman R R 2002 *Phys. Rev. Lett.* **88** 215006
[7] Fuchs J *et al* 2007 *Phys. Plasmas* **14** 053105
[8] Hey D S *et al* 2009 *Phys. Plasmas* **16** 123108
[9] Kaluza M, Schreiber J, Santala M I K, Tsakiris G D, Eidmann K, Meyer-ter Vehn J and Witte K J 2004 *Phys. Rev. Lett.* **93** 045003
[10] Fuchs J *et al* 2006 *Nat. Phys.* **2** 48
[11] Sentoku Y *et al* 2000 *Phys. Rev.* E **62** 7271
[12] Robinson A P L, Zepf M, Kar S, Evans R G and Bellei C 2008 *New J. Phys.* **10** 013021
[13] Qiao B, Zepf M, Gibbon P, Borghesi M, Dromey B, Kar S, Schreiber J and Geissler M 2011 *Phys. Plasmas* **18** 043102
[14] Yin L, Albright B J, Hegelich B M, Bowers K J, Flippo K A, Kwan T J T and Fernández J C 2007 *Phys. Plasmas* **14** 056706
[15] Henig A *et al* 2009 *Phys. Rev. Lett.* **103** 045002
[16] Bulanov S S *et al* 2008 *Phys. Rev.* E **78** 026412
[17] Nakamura T, Bulanov S V, Esirkepov T Z and Kando M 2010 *Phys. Rev. Lett.* **105** 135002
[18] Haberberger D, Tochitsky S, Fiuza F, Gong C, Fonseca R A, Silva L O, Mori W B and Joshi C 2012 *Nat. Phys.* **8** 95
[19] Hegelich B M *et al* 2011 *Nucl. Fusion* **51** 083011
[20] Kar S *et al* 2012 *Phys. Rev. Lett.* **109** 185006
[21] Jung D *et al* 2013 *New J. Phys.* **15** 023007
[22] Hegelich B M *et al* 2013 *New J. Phys.* **15** 085015
[23] McKenna P *et al* 2004 *Phys. Rev.* E **70** 036405
[24] Palaniyappan S, Huang C, Gautier D C, Hamilton C E, Santiago M A, Kreuzer C, Sefkow A B, Shah R C and Fernández J C 2015 *Nat. Commun.* **6** 10170
[25] Braenzel J, Andreev A A, Platonov K, Klingsporn M, Ehrentraut L, Sandner W and Schnürer M 2015 *Phys. Rev. Lett.* **114** 124801
[26] Wu D, Qiao B, McGuffey C, He X T and Beg F N 2014 *Phys. Plasmas* **21** 123118
[27] Yanovsky V *et al* 2008 *Opt. Express* **16** 2109
[28] Dollar F *et al* 2011 *Phys. Rev. Lett.* **107** 065003
[29] Dollar F *et al* 2012 *Phys. Rev. Lett.* **108** 175005
[30] Moore C E 1970 Ionization potentials and ionization limits derived from the analyses of optical spectra *Technical Report* No. NSRDS-NBS-34 DTIC Document National Standard Reference Data System
[31] Penetrante B M and Bardsley J N 1991 *Phys. Rev.* A **43** 3100
[32] Schreiber J *et al* 2006 *Phys. Rev. Lett.* **97** 045005
[33] Petrov G M and Davis J 2011 *Phys. Plasmas* **18** 073102
[34] Ammosov M, Delone N and Krainov V 1986 *Sov. Phys.—JETP* **64** 1191
[35] Lotz W 1970 *J. Opt. Soc. Am.* **60** 206
[36] Petrov G M, Davis J and Petrova T 2009 *Plasma Phys. Control. Fusion* **51** 095005
[37] Kemp A J, Pfund R E W and Meyer-ter Vehn J 2004 *Phys. Plasmas* **11** 5648
[38] Wilks S C, Kruer W L, Tabak M and Langdon A B 1992 *Phys. Rev. Lett.* **69** 1383
[39] Pukhov A and Meyer-ter Vehn J 1997 *Phys. Rev. Lett.* **79** 2686
[40] Neely D, Foster P, Robinson A, Lindau F, Lundh O, Persson A, Wahlström C-G and McKenna P 2006 *Appl. Phys. Lett.* **89** 021502
[41] d'Humières E, Lefebvre E, Gremillet L and Malka V 2005 *Phys. Plasmas* **12** 062704